

Multi-Ray Channel Modeling and Wideband Characterization for Wireless Communications in the Terahertz Band

Chong Han, *Student Member, IEEE*, A. Ozan Bicen, *Student Member, IEEE*, and Ian F. Akyildiz, *Fellow, IEEE*

Abstract—Terahertz (0.06–10 THz) Band communication is envisioned as a key technology for satisfying the increasing demand for ultra-high-speed wireless links. In this paper, first, a unified multi-ray channel model in the THz Band is developed based on ray tracing techniques, which incorporates the propagation models for the line-of-sight, reflected, scattered, and diffracted paths. The developed theoretical model is validated with the experimental measurements (0.06–1 THz) from the literature. Then, using the developed propagation models, an in-depth analysis on the THz channel characteristics is carried out. In particular, the distance-varying and frequency-selective nature of the Terahertz channel is analyzed. Moreover, the coherence bandwidth and the significance of the delay spread are studied. Furthermore, the wideband channel capacity using flat and water-filling power allocation strategies is characterized. Additionally, the temporal broadening effects of the Terahertz channel are studied. Finally, distance-adaptive and multi-carrier transmissions are suggested to best benefit from the unique relationship between distance and bandwidth. The provided analysis lays out the foundation for reliable and efficient ultra-high-speed wireless communications in the (0.06–10) THz Band.

Index Terms—Terahertz band, ray-tracing, multi-ray channel modeling, multipath effects, wideband.

I. INTRODUCTION

WIRELESS data traffic has exponentially grown in the past years, and this has been accompanied by an increasing demand for higher speed wireless communication. In particular, wireless data rates have doubled every eighteen months over the last three decades and are currently approaching the capacity of wired communication systems, [1]. Advanced physical layer solutions and, more importantly, new spectral bands will be required to support this high data rate for future wireless communications. Amongst others, the Terahertz (0.06–10 THz) Band is identified as one of the promising spectrum bands to enable ultra-high-speed communications [2].

Manuscript received March 25, 2014; revised October 1, 2014; accepted December 19, 2014. Date of publication December 29, 2014; date of current version May 7, 2015. This work was supported by the U.S. National Science Foundation (NSF) under Grant No. CCF-1349828 and in part by Alexander von Humboldt Foundation through Ian Akyildiz's Humboldt Research Prize in Germany. The associate editor coordinating the review of this paper and approving it for publication was L. Liu.

The authors are all with the Broadband Wireless Networking Laboratory (BWN-Lab), School of Electrical and Computer Engineering, Georgia Institute of Technology, Atlanta, GA 30332 USA (e-mail: chong.han@ece.gatech.edu; bozan@ece.gatech.edu; ian@ece.gatech.edu).

Color versions of one or more of the figures in this paper are available online at <http://ieeexplore.ieee.org>.

Digital Object Identifier 10.1109/TWC.2014.2386335

The THz Band offers a very broad bandwidth, which ranges from tens of GHz up to several THz depending on the transmission distance. Recently, the Terahertz technologies are rapidly advancing, and the development of new transceiver architectures and antennas built upon novel materials are bringing THz Band communication one step closer to the reality [3]. The use of this frequency band is envisioned to address the spectrum scarcity and capacity limitations of current wireless systems, and boost a plethora of applications, including ultra-high-speed wireless backhaul to the small cells, ultra-high-speed data transfers among proximal devices, and secure wireless communication for military applications.

For the realization of optimal wireless communication networks in the THz Band, it is imperative to develop a unified channel model which accurately characterizes the Terahertz spectrum peculiarities. The challenges and requirements to be addressed for the analysis and design of THz Band channels can be summarized as follows:

- *Modeling the multi-ray propagation:* The multi-ray propagation is present in many common scenarios. A unified multi-ray model for the entire Terahertz spectrum needs to be developed, which incorporates the accurate characterization of the line-of-sight (LoS), reflected, scattered and diffracted paths.
- *Analyzing the channel characteristics:* The channel parameters of the Terahertz spectrum such as the path gain, the wideband channel capacity, the rms delay spread and the temporal broadening effects need to be accurately investigated. These parameters are influenced by multiple factors including the operating frequency, communication distance and the material properties of the environment.

These challenges need to be addressed to realize the design of efficient and reliable ultra-high-speed wireless communications in the THz Band. The existing channel models for the lower frequency bands such as 60 GHz [4] or ultra-wideband (3.1–10.6 GHz) [5] do not capture the behavior of the THz Band, such as the very high molecular absorption loss or the very high reflection loss. The few channel models in the THz Band to date [6]–[10] are aimed at characterizing the multipath channel at 0.3 THz, as the experimental measurements are readily available. These models capture the peculiarities of the EM wave transmission in the THz Band, including the molecular absorption effect of direct ray propagation and the scattering loss of rough surfaces in indirect ray communication. However, they are mainly based on measurements, which are strictly

subject to the specific indoor environment settings. Moreover, a stochastic 0.3 THz indoor channel model is introduced in [11], which provides a scenario-specific parameter set for the considered environment. Nevertheless, the thorough analysis for the wideband channel characteristics is missing. Hence, there is a need for a unified multi-ray propagation model with thorough understanding and analysis of the entire Terahertz spectrum to lay out the foundation for reliable and efficient wireless communications in the THz Band.

In this paper, we develop a unified multi-ray channel model in the (0.06–10) THz Band based on ray tracing techniques using a bottom-up approach. The developed theoretical model is validated with the experimental measurements (0.06–1 THz) from the literature. Using the developed propagation models, we present an in-depth analysis on the channel characteristics in the THz Band. This work lays out the foundation for reliable and efficient wireless communications in the THz Band. The distinctive features of our work are summarized as follows:

- **We develop an analytical multi-ray channel model based on ray tracing techniques, as a superposition of LoS, reflected, scattered and diffracted paths.** The developed model is unified in the (0.06–10) THz Band, while the evaluation and validation of the model are limited up to 1 THz where the parameters of material properties are readily available.
- **We present an in-depth analysis on the channel characteristics in the THz Band.** Specifically, we analyze the distance-varying and frequency-selective nature of the Terahertz channel. Moreover, we study the coherence bandwidth, and point out the significance of the delay spread. Furthermore, we characterize the wideband channel capacity using flat and water-filling power allocation strategies. Additionally, we analyze the temporal broadening effects of the Terahertz channel. Finally, we advocate for distance-adaptive and multi-carrier transmissions to best benefit from the unique relationship between distance and bandwidth.

The remainder of this paper is organized as follows. In Section II, the multi-ray propagation model in the THz Band is developed in a bottom-up fashion. Moreover, the validation for the developed model is provided. Then, in Section III, the characteristics of the wireless channel are analyzed by using the developed models. In particular, the distance-varying spectral windows, wideband channel capacity, delay spread, temporal broadening and the impact on communication techniques are presented, respectively. Finally, the paper is concluded in Section IV.

II. ELECTROMAGNETIC WAVE PROPAGATION IN THE THZ BAND: A MULTI-RAY MODEL

In this section, we use the ray tracing techniques to develop the multi-ray channel model, by utilizing the principles of geometric optics to trace the propagation of LoS, reflected, diffusely scattered and diffracted EM waves. The very short wavelength in the THz Band allows accurate modeling with this ray optical approach. In particular, ray tracing methods have been proved to enable very good prediction capabilities

at 60 GHz as well as low Terahertz frequency at 0.3 THz [6]. Due to the lack of experimental characterization of the material properties for NLoS propagation at high THz frequencies, i.e., 1–10 THz, the validation and the characteristics analysis are focused on the lower THz Band, i.e., 0.06 to 1 THz, although the multi-ray approach is unified. When the material parameters are made available, our unified and analytical multi-ray approach can also be utilized to investigate higher THz frequencies.

Since the frequency dependency appears in the propagation channel and antennas in the THz Band, we develop a multi-ray propagation model in the THz Band as the combination of many individual sub-bands [5]. Each sub-band is considered to be narrow enough to have flat frequency response. In the i^{th} frequency sub-band, the narrowband channel impulse response is expressed as a superposition of N_i rays, among which the n^{th} ray experiences frequency-dependent attenuation $\alpha_{i,n}$. By denoting t as the time when impulse response is observed, and τ as the propagation delay, the channel response of the multi-ray model is given by

$$h_i(\tau, t) = \sum_{n=1}^{N_i(t)} \alpha_{i,n}(t) \delta(\tau - \tau_n), \quad (1)$$

where $\tau_n = \frac{r_n}{c}$ is the delay of the n^{th} path. r_n refers to the traveling distance and c stands for the speed of light.

For any fixed transmitter and receiver locations and stationary environment, the time parameter can be omitted in the model. The time-invariant assumption changes the above model to

$$h_i(\tau) = \sum_{n=1}^{N_i} \alpha_{i,n} \delta(\tau - \tau_n). \quad (2)$$

The multi-ray propagation consists of LoS, reflected, scattered, and diffracted paths, which are demonstrated in Fig. 1. If there are $N_{\text{Ref}}^{(i)}$ reflected rays, $N_{\text{Sca}}^{(i)}$ scattered rays, and $N_{\text{Dif}}^{(i)}$ diffracted rays in the i^{th} frequency sub-band, the multi-ray channel model can be described as

$$h_i(\tau) = \alpha_{\text{LoS}}^{(i)} \delta(\tau - \tau_{\text{LoS}}) \mathbb{1}_{\text{LoS}} + \sum_{p=1}^{N_{\text{Ref}}^{(i)}} \alpha_{\text{Ref}}^{(i,p)} \delta(\tau - \tau_{\text{Ref}}^{(p)}) + \sum_{q=1}^{N_{\text{Sca}}^{(i)}} \alpha_{\text{Sca}}^{(i,q)} \delta(\tau - \tau_{\text{Sca}}^{(q)}) + \sum_{u=1}^{N_{\text{Dif}}^{(i)}} \alpha_{\text{Dif}}^{(i,u)} \delta(\tau - \tau_{\text{Dif}}^{(u)}), \quad (3)$$

where $\mathbb{1}_{\text{LoS}}$ is the indicator function that is equal to 1 or 0 for the presence of LoS path or not. For the LoS path, $\alpha_{\text{LoS}}^{(i)}$ refers to the attenuation, and τ_{LoS} stands for the delay. For the p^{th} reflected path, $\alpha_{\text{Ref}}^{(i,p)}$ is the attenuation and $\tau_{\text{Ref}}^{(p)}$ is the delay. Similarly for the q^{th} scattered path and u^{th} diffracted path, the attenuations are expressed as $\alpha_{\text{Sca}}^{(i,q)}$ and $\alpha_{\text{Dif}}^{(i,u)}$, while the delays are denoted by $\tau_{\text{Sca}}^{(q)}$ and $\tau_{\text{Dif}}^{(u)}$, respectively.

By invoking the Wiener-Khinchin theorem, the attenuations and delays in the i^{th} frequency sub-band can be written as

$$\begin{pmatrix} \alpha_{\text{LoS}}^{(i)} \\ \alpha_{\text{Ref}}^{(i,p)} \\ \alpha_{\text{Sca}}^{(i,q)} \\ \alpha_{\text{Dif}}^{(i,u)} \end{pmatrix} = \begin{pmatrix} |H_{\text{LoS}}(f_i)| \\ H_{\text{Ref}}^{(p)}(f_i) \\ H_{\text{Sca}}^{(q)}(f_i) \\ H_{\text{Dif}}^{(u)}(f_i) \end{pmatrix}, \quad (4)$$

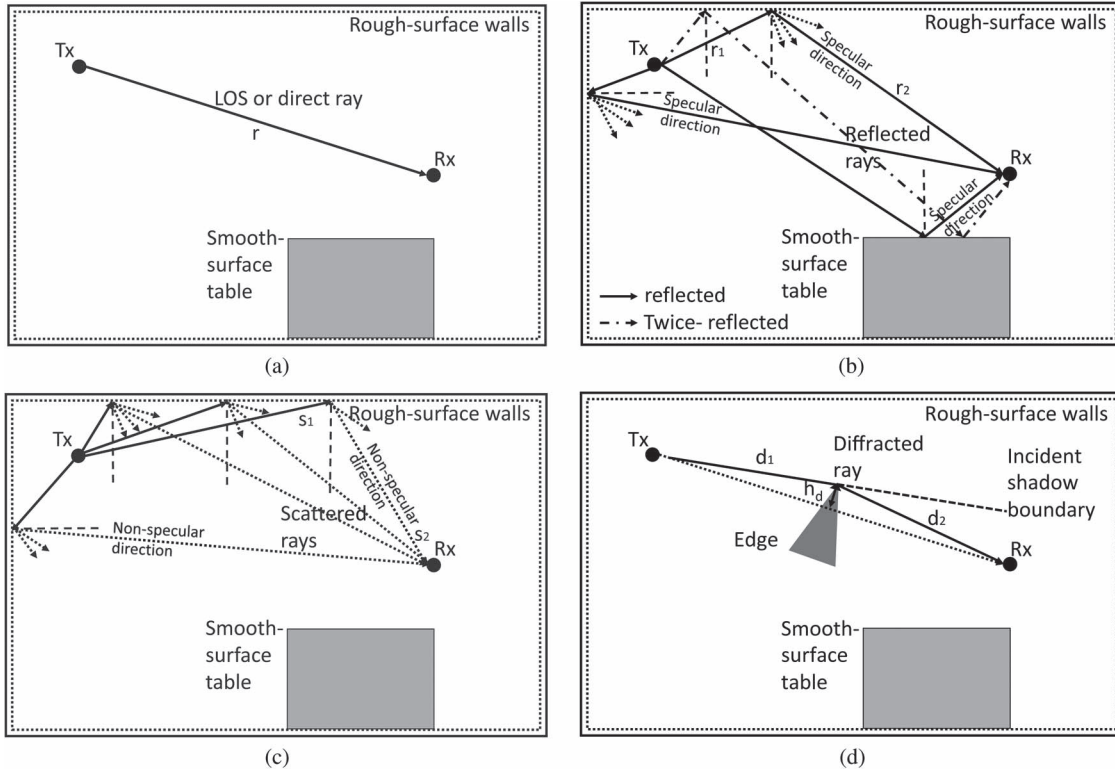


Fig. 1. Propagation models between the transmitter (Tx) and the receiver (Rx). (a) Line-of-sight or direct ray propagation. (b) Reflected ray propagation. (c) Scattered ray propagation. (d) Diffracted ray propagation.

where H_{LoS} , $H_{\text{Ref}}^{(p)}$, $H_{\text{Sca}}^{(q)}$, and $H_{\text{Dif}}^{(u)}$ are the transfer functions for the LoS, reflected, scattered and diffracted propagation paths, respectively. In the i^{th} frequency sub-band, the center frequency is denoted by f_i . In the following, we describe the mathematical framework to characterize the different single propagation path, as a function of the frequency, f .

A. LoS Propagation in the THz Band

The free space direct ray or LoS channel transfer function, H_{LoS} , consists of the spreading loss function, H_{Spr} , and the molecular absorption loss function, H_{Abs} , as

$$H_{\text{LoS}}(f) = H_{\text{Spr}}(f)H_{\text{Abs}}(f)e^{-j2\pi f\tau_{\text{LoS}}}. \quad (5)$$

The transfer function due to the spreading loss is given by

$$H_{\text{Spr}}(f) = \frac{c}{4\pi \cdot f \cdot r}. \quad (6)$$

The transfer function of the molecular absorption loss has the form

$$H_{\text{Abs}}(f) = e^{-\frac{1}{2}k(f)r}, \quad (7)$$

where c denotes the speed of light, r stands for the distance between the transmitter and the receiver, and $\tau_{\text{LoS}} = r/c$ equals to the time-of-arrival of the LoS propagation. The absorption loss in (7) accounts for the attenuation that part of the wave energy is converted into internal kinetic energy to the molecules in the propagation medium, and can be computed by using the Beer-Lambert law. In particular, k is the frequency-dependent medium absorption coefficient, and depends on the composition

of the transmission medium at a molecular level. This absorption loss is characterized as

$$k(f) = \sum_q \frac{p}{p_0} \frac{T_{\text{STP}}}{T} Q^q \sigma^q(f), \quad (8)$$

where p refers to the system pressure in Kelvin, p_0 is the reference pressure, T_{STP} is the temperature at standard pressure, Q^q is the number of molecules per volume unit of gas q and σ^q is the absorption cross-section of gas q . In particular, the contributions to molecular absorption from oxygen, carbon dioxide, methane, nitrogen dioxide, ozone, nitrous oxide, carbon monoxide, and water vapor are considered. Among others, the major contribution to the total absorption in a regular medium in the THz Band comes from the molecules of water vapor. More detailed analysis on the molecular absorption effect can be found in [12].

B. Multipath Propagation Effects

A major challenge in non-line-of-sight propagation is the rough surface roughness. In the THz Band, any surface with roughness comparable to the wavelength (i.e., millimeter or sub-millimeter) scatters the EM wave. As a result, surfaces that are considered smooth at lower-frequencies wireless communication become rough in the THz Band.

For rough surfaces, the backscattered EM wave on a surface consists of the the *reflected or coherent ray* in the specular direction, as well as the *scattered or incoherent rays* in all other directions [Fig. 1(b) and 1(c)]. In addition, another multipath effect is the *diffraction* as shown in Fig. 1(d). The transfer functions for the reflected, scattered and diffracted ray propagation are described in the following.

1) *Reflected Ray Propagation*: If we denote R as the reflection coefficient, r_1 as the distance between the transmitter and the reflector, and r_2 as the distance between the reflector and the receiver, then the frequency-dependent transfer function of the reflected ray propagation, H_{Ref} , is given by

$$H_{\text{Ref}}(f) = \left(\frac{c}{4\pi \cdot f \cdot (r_1 + r_2)} \right) e^{-j2\pi f \tau_{\text{Ref}} - \frac{1}{2}k(f)(r_1 + r_2)} \cdot R(f), \quad (9)$$

where $\tau_{\text{Ref}} = \tau_{\text{LoS}} + (r_1 + r_2 - r)/c$ is the time-of-arrival of the reflected ray.

In the above equation, the rough surface reflection loss of EM waves at THz Band frequencies needs to be computed, which depends on the material, the shape and the roughness of the surface on which EM waves have been reflected. Without loss of generality, we consider the Transverse Electric (TE) part of the EM wave (i.e., perpendicular to the plane of incidence), while Transverse Magnetic (TM) part (i.e., parallel to the plane of incidence) can be extended in a similar fashion. Since the problem of wave scattering from rough surfaces has no closed-form solutions existing to date, approximation solutions are adopted for many practical applications. We use the Kirchhoff theory to capture the reflection loss in the specular reflection, since this approximation technique is applicable to a surface with correlation length much greater than a wavelength in the THz Band. Alternative common approximation method is the small perturbation model [13], which assumes the variation in surface height is small compared to the wavelength. This assumption is inappropriate for EM waves with very small wavelength in the THz Band.

Hence, according to the Kirchhoff scattering theory, the reflection coefficient for a rough surface can be obtained by multiplying the smooth surface reflection coefficient derived from the Fresnel equations, γ_{TE} , with the *Rayleigh roughness factor*, ρ , as

$$R(f) = \gamma_{\text{TE}}(f) \cdot \rho(f). \quad (10)$$

The Fresnel reflection coefficient for TE polarized waves on a smooth surface is obtained as

$$\begin{aligned} \gamma_{\text{TE}}(f) &= \frac{\cos(\theta_i) - n_t \sqrt{1 - \left(\frac{1}{n_t} \sin(\theta_i)\right)^2}}{\cos(\theta_i) + n_t \sqrt{1 - \left(\frac{1}{n_t} \sin(\theta_i)\right)^2}} \\ &= - \left(1 + \frac{-2\cos(\theta_i)}{\cos(\theta_i) + \sqrt{n_t^2 - \sin^2(\theta_i)}} \right) \\ &\approx - \left(1 + \frac{-2\cos(\theta_i)}{\sqrt{n_t^2 - 1}} \right) \\ &\approx - \exp\left(\frac{-2\cos(\theta_i)}{\sqrt{n_t^2 - 1}}\right), \end{aligned} \quad (11)$$

where θ_i is the angle of incident wave and can be computed using the law of cosine and to the locations of the transmitter, the receiver and the reflection point. Specifically, $\theta_i = \frac{1}{2} \cos^{-1} \left(\frac{r_1^2 + r_2^2 - r^2}{2r_1 r_2} \right)$, where r_1 is the distance between the transmitter and the reflection point, r_2 is the distance between

the reflection point and the receiver, and r is the distance between the transmitter and the receiver. Moreover, n_t refers to the refractive index, which varies with the frequencies and medium material [14]. As we consider the reflected rays with large incident angles, the Taylor's approximation for the smooth surface reflection coefficient in (11) shows good accuracy at Terahertz frequencies. The negative sign shows a phase change of π caused in reflection.

Moreover, a statistical parameter for roughness is the rough surface height standard deviation, σ , which is commonly considered to be Gaussian-distributed. This roughness effect is characterized by a Rayleigh factor [15], as

$$\rho(f) = \exp\left(-\frac{8\pi^2 \cdot f^2 \cdot \sigma^2 \cdot \cos^2(\theta_i)}{c^2}\right). \quad (12)$$

2) *Scattered Ray Propagation Model*: In the THz Band, the wavelength is at the order of millimeters or below, which results in diffuse scattering very critical in channel modeling. The impact of scattering increases with higher roughness level. Similarly in the specular reflected model, we consider the scattering on a surface with a Gaussian-like height distribution, where sharp irregularities are not present if the correlation length of the rough surface, L , is larger than the wavelength. We denote S as the scattering coefficient for a rough surface, s_1 as the distance between the transmitter and the scattering point, and s_2 as the distance between the scattering point and the receiver. Then the transfer function of the scattered ray propagation, H_{Sca} , is given by

$$H_{\text{Sca}}(f) = \left(\frac{c}{4\pi \cdot f \cdot (s_1 + s_2)} \right) e^{-j2\pi f \tau_{\text{Sca}} - \frac{1}{2}k(f)(s_1 + s_2)} \cdot S(f), \quad (13)$$

where $\tau_{\text{Sca}} = \tau_{\text{LoS}} + (s_1 + s_2 - r)/c$ is the time-of-arrival of the scattered ray. The scattering geometry is considered on the tangent plane (the incident azimuth angle ϕ_1 is π), and θ_1 stands for the zenith angle of the incident wave. In addition, θ_2 and ϕ_2 denote the zenith and azimuth angle of the scattered wave, respectively.

The classic Kirchhoff theory is based on a paraxial (small-angle) assumption, which limits its ability to accurately account for large angles of incidence. Instead, the scattering coefficient of rough surfaces according to the modified Beckmann-Kirchhoff theory [16] shows good experimental agreement for rough surfaces at large angles of incidence and large scattering angles, which is given by

$$\begin{aligned} S(f) &= \gamma_{\text{TE}}(f) \cdot e^{-\frac{g}{2}} \cdot \sqrt{\rho_0^2 + \frac{\pi L^2 F^2}{l_x l_y} \sum_{m=1}^{\infty} \frac{g^m}{m!m} e^{-v_s/m}} \\ &= \gamma_{\text{TE}}(f) \cdot \sqrt{\frac{1}{e^g}} \cdot \sqrt{\rho_0^2 + \frac{\pi L^2 F^2}{l_x l_y} \sum_{m=1}^{\infty} \frac{g^m}{m!m} e^{-v_s/m}} \\ &\approx - \exp\left(\frac{-2\cos(\theta_1)}{\sqrt{n_t^2 - 1}}\right) \cdot \sqrt{\frac{1}{1 + g + \frac{g^2}{2} + \frac{g^3}{6}}} \\ &\quad \cdot \sqrt{\rho_0^2 + \frac{\pi \cos(\theta_1)}{100} \left(g e^{-v_s} + \frac{g^2}{4} e^{-v_s/2} \right)} \end{aligned} \quad (14)$$

In the above derivations, we used Taylor's approximation to simplify the expression for the scattering coefficient. As the frequency increases, the Fresnel reflection coefficient, γ_{TE} , decreases, while the summation term increases. This explains why the scattering coefficient is not monotonically decreases with the frequency. Detailed computations for the parameters including $g, \rho_0, l_x, l_y, v_x, v_y, v_s$ can be found in [17].

3) *Diffacted Ray Propagation Model*: In the THz Band, the diffraction effect is negligible for most of the cases, particularly for indoor environment. The only exception is the region close to the incident shadow boundary, under NLoS conditions. Although diffraction can be accurately characterized using the Uniform geometrical Theory of Diffraction (UTD) [18], the complexity of this approach is very high and it requires numerical solutions for path loss. For simplicity, we use the Fresnel Knife Edge Diffraction (KED) theory [19] to provide approximated characterization for diffraction. In particular, this model considers very thin diffracting object and neglects the diffractor parameters such as polarization, conductivity, and surface roughness, which can lead to inaccuracies. Hence, frequency-dependent coefficients μ_1, μ_2, μ_3 are used to tailor the Fresnel KED model for THz Band communication.

The diffraction coefficient, $L(f)$, characterizes the loss that is created in addition to the LoS propagation attenuation. By incorporating this diffraction loss, the diffraction channel transfer function, H_{Dif} , is given by

$$H_{Dif}(f) = \left(\frac{c}{4\pi \cdot f \cdot (d_1 + d_2)} \right) e^{-j2\pi f \tau_{Dif} - \frac{1}{2}k(f)(d_1 + d_2)} \cdot L(f), \quad (15)$$

where d_1 as the distance between the transmitter and the diffracting point, d_2 as the distance between the diffracting point and the receiver, and $\tau_{Dif} = \tau_{LoS} + \Delta d/c$ is the time-of-arrival of the diffracted ray. In a common diffraction geometry where h_d [see Fig. 1(d)] is small relative to d_1 and d_2 ,

the diffracted signal travels an additional distance relative to the LoS path of approximately

$$\Delta d = \frac{h_d^2(d_1 + d_2)}{2d_1d_2}. \quad (16)$$

Moreover, the diffraction angle that lies between the incident shadow boundary and the diffracted path to Rx is computed as $\theta_d = 180^\circ - \cos^{-1}(\frac{h_d}{d_1}) - \cos^{-1}(\frac{h_d}{d_2})$. If we define $v(f) = \sqrt{\frac{2f\Delta d}{c}}$, the diffraction coefficient can be obtained by an approximation to the Fresnel integral, as

$$L(f) = \begin{cases} \mu_1(f) \cdot (0.5e^{-0.95v(f)}) & 0 < v \leq 1, \\ \mu_2(f) \cdot (0.4 - \sqrt{0.12 - (0.38 - 0.1v(f))^2}) & 1 < v \leq 2.4, \\ \mu_3(f) \cdot (0.225/v(f)) & v > 2.4, \end{cases} \quad (17)$$

where the frequency-dependent parameters μ_1, μ_2, μ_3 are chosen to best fit the empirical data in [21].

C. Overall Multi-Ray Model for THz Band Wireless Communication

By combining the aforementioned models in (5), (9), (13), and (15), the multi-ray model in the i^{th} frequency sub-band in (3) can be rearranged in (18), shown at the bottom of the page.

D. Validation of Multi-Ray Model With Experimental Measurements

In this section, we validate the developed multipath channel model with the existed experimental measurements, at 60 GHz [4], 0.3 THz and up to 1 THz [15], [20], [21]. The developed multi-ray channel model is unified in the (0.06–10) THz Band, although the validation and evaluation are up to 1 THz limited by the available parameter measurements.

$$\begin{aligned} h_i(\tau) = & \left| \frac{c}{4\pi \cdot f_i \cdot r} e^{-\frac{1}{2}k(f_i)r} \right| \cdot \delta(\tau - \tau_{LoS}) \mathbb{1}_{LoS} \\ & + \sum_{p=1}^{N_{Ref}^{(i)}} \left| \left(\frac{c}{4\pi \cdot f_i \cdot (r_1 + r_2)} \right) e^{-\frac{1}{2}k(f_i)(r_1 + r_2)} \cdot \left(-e^{\frac{-2\cos(\theta_1)}{\sqrt{n_r^2 - 1}}} \right) e^{-\frac{8\pi^2 \cdot f_i^2 \cdot \sigma^2 \cdot \cos^2(\theta_1)}{c^2}} \right| \cdot \delta(\tau - \tau_{Ref}^{(p)}) \\ & + \sum_{q=1}^{N_{Sca}^{(i)}} \left| \left(\frac{c}{4\pi \cdot f_i \cdot (s_1 + s_2)} \right) e^{-\frac{1}{2}k(f_i)(s_1 + s_2)} \cdot \left(-e^{\frac{-2\cos(\theta_1)}{\sqrt{n_r^2 - 1}}} \right) \cdot \sqrt{\frac{1}{1 + g + \frac{g^2}{2} + \frac{g^3}{6}}} \right|_q \\ & \cdot \left| \sqrt{\rho_0^2 + \frac{\pi \cos(\theta_1)}{100} \left(g e^{-v_s} + \frac{g^2}{4} e^{-v_s/2} \right)} \right|_q \cdot \delta(\tau - \tau_{Sca}^{(q)}) \\ & + \sum_{u=1}^{N_{Dif}^{(i)}} \left| \left(\frac{c}{4\pi \cdot f_i \cdot (d_1 + d_2)} \right) e^{-\frac{1}{2}k(f_i)(d_1 + d_2)} \cdot L(f_i) \right|_u \cdot \delta(\tau - \tau_{Dif}^{(u)}) \end{aligned} \quad (18)$$

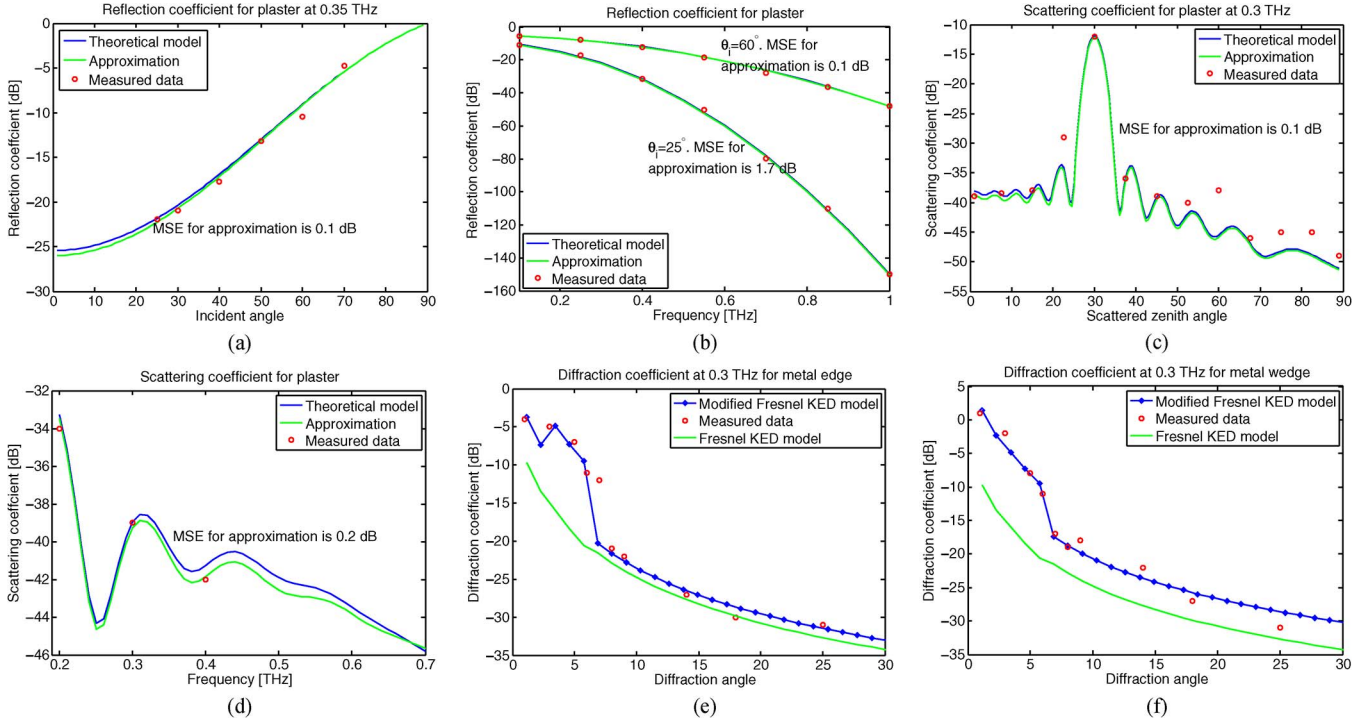


Fig. 2. Validation for reflection, scattering and diffraction coefficients. (a) Reflection coefficient vs. incident angle. Measured data is from [15]. (b) Reflection coefficient vs. frequency. Measured data is from [15]. (c) Scattering coefficient vs. scattered zenith angle. Measured data is from [21]. (d) Scattering coefficient vs. frequency. Measured data is from [21]. (e) Diffraction coefficient for metal edge. Measured data is from [20]. (f) Diffraction coefficient for metal wedge. Measured data is from [20].

The received signal in a multi-ray channel is contributed by not only the LoS path, but also non-line-of-sight (NLoS), which includes the reflected, scattered and diffracted rays. As a result, the coefficients for reflection, scattering and diffraction from our derivations, are validated with the measured data first. Ultimately, the sub-band multi-ray model is validated.

1) *Reflection Coefficient*: The reflection coefficients for the plaster are characterized, as a function of the incident angle and the frequency, respectively, in Fig. 2(a) and (b). In particular, more energy is lost as the incident wave approaches the perpendicular to the surface, i.e., incident angle approaches zero. Moreover, the reflection loss is more severe for larger frequencies, because the level of roughness rises as the wavelength drops. In these figures, the theoretical model in (10), the approximation using (11), and the measured data from [15] are plotted for comparison. Furthermore, the mean square error (MSE) between the theoretical model and its approximation is computed to quantitatively evaluate the approximation. These results show very good accuracy of modeling and approximation have been obtained, particularly for large incident angles.

2) *Scattering Coefficient*: The theoretical models and the approximation for scattering coefficients are verified. By fixing the frequency at 0.3 THz, incident zenith angle at $\theta_1 = 30^\circ$ and the scattered azimuth angle at $\phi_2 = 0^\circ$, the scattering coefficient for the plaster is shown as a function of the scattered zenith angle θ_2 , in Fig. 2(c). The parameter values used in (14) include: the refractive index $n_t = 2.24 - j0.025$, the rough surface height standard deviation $\sigma = 0.088$ mm, and the correlation length $L = 0.18$ mm [21]. The approximation shows a reasonable agreement with the theoretical model and the measurements.

Next, by fixing the scattered zenith angle, the scattering loss rises with the frequency non-monotonically up to 0.7 THz, as shown in Fig. 2(d). The scattering angles are selected as $\theta_1 = 30^\circ$, $\theta_2 = 45^\circ$, and $\phi_2 = 0^\circ$. The approximation in (14) has very small MSE of 0.2 dB over the frequency range up to 0.7 THz, compared to the theoretical model by modified Beckmann-Kirchhoff theory.

3) *Diffraction Coefficient*: The diffraction coefficients are evaluated using the modified KED model in (17), the measured data [19] and the KED model. In Fig. 2(e) and (f), the diffraction coefficients for the metal edge and the metal wedge are plotted individually. Because of the lacking for consideration of material properties, the KED model is not as accurate as the modified KED model in (17). In particular, we compute the parameters $[\mu_1, \mu_2, \mu_3]$ as [2, 3.6, 1.15] for the metal edge, and [3.6, 3.6, 1.6] for the metal wedge, which are obtained based on the empirical experiments. The increasing of diffraction loss for larger diffraction angle α_d is well captured by the modified KED model.

4) *Multi-Ray Model*: Ultimately, we validate our multi-ray propagation model in (18) with the experimental measurements conducted in a room of dimensions 5 m \times 2.75 m \times 2.5 m, in which there are two tables separated by a screen [21]. The transmitter Tx is placed under the ceiling to obtain a large coverage of the room, while the two receivers are placed on the two tables.

In Case 1, the receiver Rx₁ has LoS path available. On the contrary, in Case 2, the receiver Rx₂ has no LoS. The walls and the ceiling are covered by plaster, where its refractive index up to 1 THz can be found in [15]. The simulation results are

TABLE I
THE SIGNIFICANT ARRIVAL RAYS AT 0.3 THZ

Arrival path	Case 1, when LoS is present		Case 2, when LoS is absent	
	Path Gain [dB]	Delay [ns]	Path Gain [dB]	Delay [ns]
LoS	-90.6	8.94	—	—
Reflected ray 1	-102.1	9.14	-102.2	14.01
Reflected ray 2	-103.4	9.77	-101.8	14.43
Reflected ray 3	-116.7	10.01	-111.3	14.58
Scattered ray 1	-125.8	9.80	-134.7	14.45
Scattered ray 2	-144.2	10.27	-134.8	14.61
Scattered ray 3	-141.7	11.08	152.5	15.66
Scattered ray 4	-134.1	12.74	-143.5	22.48
Diffracted ray 1	—	—	-125.9	14.03

summarized in Table I, which include the type of arrival path, the path gain and the delay. These results are validated with the measured values at 0.3 THz in [20], [21]. The observations are summarized as follows.

- *Case 1: LoS is present.* The distance between Tx and Rx₁ is 3 m. When $f_i = 0.3$ THz, the LoS ray arrives at 8.94 ns with the power -90.6 dB. The total gain reaches -86.5 dB, which suggests a 4.1 dB improvement to have multipath propagation. In this simulation, the LoS, the once-reflected, the twice-reflected and the scattered rays are included.
- *Case 2: LoS is absent.* The distance between Tx and Rx₂ is 4 m. The once-reflected, the twice-reflected, the relevant scattered and the diffracted rays are included in this simulation. The strongest reflected ray travels through the ceiling, arriving at 14.43 ns with the path gain -101.8 dB. The total gain by including multipath propagation is -94.2 dB, which is 7.6 dB improvement compared to the single NLoS transmission. Moreover, the diffracted path is included in our simulation, having a delay of 14.03 ns and a path gain of -125.9 dB.

E. Discussion

The developed narrowband channel model considers that the system bandwidth is narrow enough so that the frequency response can be treated as a complex valued scalar over the whole bandwidth, the so-called frequency-flat channel. Then, we develop a multi-ray propagation model in the THz Band as a combination of these individual sub-bands. In each sub-band, the multi-ray model is a superposition of the LoS, reflected, scattered and diffracted paths.

The principles to develop efficient multi-ray model are summarized here. When LoS is available, the direct ray dominates the received signal energy, while the reflected rays play a dominant role when LoS is absent. As the operating frequency increases, the surface is seen to be rougher and hence, more power is scattered out of the specular direction. Hence, scattered rays are very important and have to be included in the ray tracing model for both LoS and NLoS conditions. Furthermore, the diffraction path can be ignored in general, only except when the receiver is in the very closed region near the incident shadow boundary.

In our analysis of the two study cases, the number of specular reflected rays is up to 6, which may include: one from the

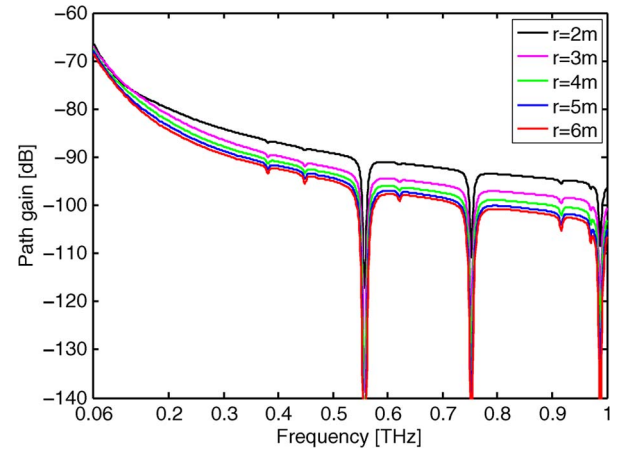


Fig. 3. Path gain as a function of frequency.

table, one from the ceiling, and four from the four walls. Moreover, the number of dominant scattered rays is 60. For each dominant reflected ray, i.e., on the table, ceiling and four walls, we consider 10 scattered rays surrounding the each reflection point. Lastly, when LoS is not available, and there is a screen or a wedge between the transmitter and the receiver, the number of diffracted ray is 1. Otherwise, the diffracted rays are negligible.

III. WIDEBAND CHARACTERIZATION

Using the developed propagation models, a detailed analysis on the wideband channel characteristics in the THz Band is presented here. Specifically, we thoroughly characterize the distance-varying spectral windows, the wideband channel capacity, the rms delay spread and the coherence bandwidth, and the temporal broadening effects in this section.

A. Distance-Varying Spectral Windows

Due to the molecular absorption effect, path loss peaks are created, and the spectral windows between these peaks are investigated, as shown in Fig. 3. In particular, three spectral windows between 0.06 THz and 1 THz can be recognized, which are 0.06–0.54 THz, 0.57–0.74 THz and 0.76–0.97 THz, respectively. As the material properties of reflection, the scattering and the diffraction properties being measured at higher Terahertz frequencies (e.g., 1–10 THz), more spectral windows can be identified in the future.

The path gain and the width of the spectral windows vary with the center frequency and the distance. First, as the center frequency increases, the channel path gain values drop, and the width of the spectral windows dwindles. The path gain separation among different distances increase for larger center frequencies. Second, the relationship between the distance and the path gain is very close, particularly for short distances. For example, when distance changes from 2 m to 3 m, the average path gain decreases from -88.3 dB to -91.4 dB. On the contrary, by increasing the distance from 5m to 6m, the path gain difference is only 1 dB, from -94.6 to -95.6 dB. Third, the available spectrum for communication reduces rapidly as the distance increases. For example, when the distance is 6m, only the frequency bands (0.06–0.54 THz) and (0.58–0.73 THz) have path loss values below 100 dB. This close relationship between the distance and the spectral windows motivates the design of distance-aware communication schemes [22].

B. Wideband Channel Capacity

To evaluate the wideband channel capacity in the THz band, we can decompose the received signal as a sum of the sub-bands, where each sub-band channel is narrow and has a flat-band response. In particular, the i^{th} sub-band is defined as $\Delta f_i = f_{i+1} - f_i$ with power P_i under the constraint $\sum_{i=1}^{N_B} P_i \leq P$, where N_B refers to the total number of sub-bands, and P stands for the total transmit power. In the i^{th} narrowband, the sub-band capacity, C_i , is expressed as

$$C_i = \Delta f_i \log \left(1 + \frac{|h_i|^2 P_i}{\Delta f_i S_N(f_i)} \right) \quad (19)$$

where S_N is the power spectral density of the additive white Gaussian noise. h_i is given in (18). Then, the wideband channel capacity in the THz Band can be found as the sum of the capacities of each sub-band [12], as

$$C = \sum_{i=1}^{N_B} \Delta f_i \log \left(1 + \frac{|h_i|^2 P_i}{\Delta f_i S_N(f_i)} \right). \quad (20)$$

By varying the total transmit power from 0 to 10 dBm, the channel capacity is numerically computed and shown in Fig. 4, for different transmission distances, different power allocation strategies and different propagation. We assume the utilized frequency band is from 0.06 THz to 1 THz, and the distance between the transmitter and the receiver is 3 m and 6 m. Using the water-filling (WF) power allocation strategy, the multipath (MP) capacity increases with the transmit power and reaches 75 Gbps at $P = 10$ dBm and $r = 3$ m. The mean capacity under these conditions is 39.9 Gbps. On the contrary, the mean capacity reduces by 89% and becomes 4.4 Gbps if the equal power (EP) allocation scheme is adopted. This suggests an importance of the intelligent resource allocation in exploiting the Terahertz spectrum due to the very high frequency-selectivity. On the other hand, the capacity decreases as the distance increases. In particular, at $r = 6$ m, the average MP capacity based on WF strategy equals to 31.4 Gbps. Furthermore, as the multipath propagation has over 4 dB gain over the LoS

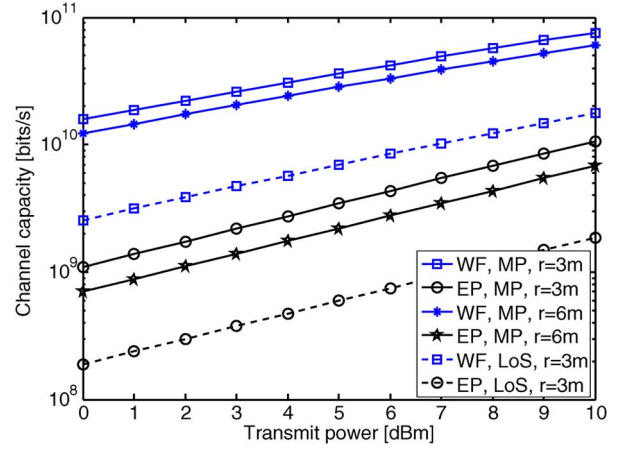


Fig. 4. Wideband channel capacity for different propagation channels and distances.

(as discussed in Section II-D4), the mean capacity of the multi-ray channel is 4.8 times that of the LoS path solely. However, this improvement of total path gain and capacity of the multipath propagation are at the costs of the increased delay spread and consequently, the restricted coherence bandwidth to avoid ISI in practice.

C. RMS Delay Spread and Coherence Bandwidth

We provide an analytical expression to compute the rms delay spread, which is a measure of how dispersive the channel is. This temporal parameter relates to the performance degradation caused by ISI and useful for the physical system design. The rms delay spread is computed as

$$\sigma_i = \sqrt{\tau_i^2 - (\bar{\tau}_i)^2}, \quad (21)$$

where

$$\bar{\tau}_i = \frac{\sum_{n=1}^N |\alpha_{i,n}|^2 \tau_n}{\sum_{n=1}^N |\alpha_{i,n}|^2}, \quad (22)$$

and

$$\tau_i^2 = \frac{\sum_{n=1}^N |\alpha_{i,n}|^2 \tau_n^2}{\sum_{n=1}^N |\alpha_{i,n}|^2}, \quad (23)$$

are the first moment (or called the mean excess delay) and second moments of the instantaneous power-delay profile, respectively. $\alpha_{i,n}$ is the amplitude of the n^{th} path in the i^{th} sub-band, as given in (2).

Regarding the power delay profile of Case 1 in Table I, the rms delay spread is calculated as 0.19 ns for $r = 3$ m. This value suggests that the symbol rate is limited to $0.1/\sigma_i = 0.53$ Gbit/s to avoid ISI for linearly-modulated signals. Moreover, the coherence bandwidth, that is defined as the range of frequencies over which channel correlation exceeds 50%, is given by $0.2/\sigma_i = 1.06$ GHz. The increasing frequency would lead to multipath effect dwindling, due to the very high loss for the NLoS paths. This results in a smaller rms delay spread and hence, larger coherence bandwidth, as shown in Fig. 5. In particular, when the distance is 3 m and the center frequency

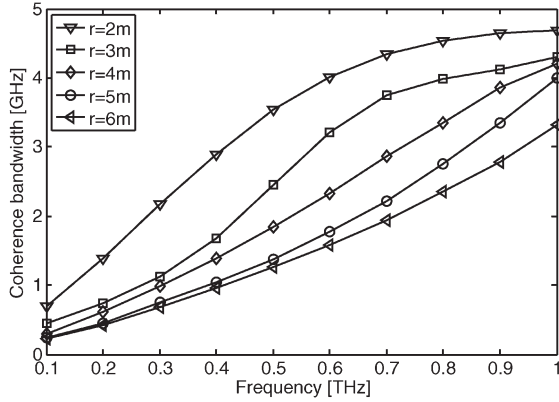


Fig. 5. Coherence bandwidth at different center frequencies.

is 0.7 THz, the rms delay spread drops to 51.7 ps, and the coherence bandwidth grows to 3.87 GHz.

As the simulation dimensions and the distance between the transmitter and the receiver increase, the ray inter-arrival times are extended. This leads to the larger rms delay spread in the multi-ray channel and therefore, the smaller coherence bandwidth in the THz Band. The average of the coherence bandwidth drops from 3.42 GHz, to 2.56 GHz, 2.17 GHz, 1.75 GHz, and 1.47 GHz, as the distance varies from 2 m, to 3 m, 4 m, 5 m, and 6 m, respectively. Moreover, as the distance increases, the convergence of the coherence bandwidth at each center frequency can be observed.

D. Temporal Broadening

The transmitted signal experiences the frequency-selectivity in the THz wideband channel, as shown in (18) and Fig. 3. This frequency-selective attenuation causes broadening effects on the transmitted signals, which restricts the minimum spacing between consecutive pulses and hence the data rates. Therefore, in this section, we present an extensive investigation of the temporal broadening effects in the THz Band. Similar broadening effects have been observed in ultra-wideband (UWB) systems [5], [23]. However, in the THz Band, the broadening effects are much stronger due to the much higher level of frequency selectivity.

An illustration of this broadening effect is shown in Fig. 6 and explained as follows. To occupy the Terahertz spectrum, a very short pulse or for simplicity, a Dirac delta function in the time domain is transmitted through the frequency-selective Terahertz channel. The Fourier transform of the Dirac delta function is flat in the frequency domain. Then, by passing through channel, the transmitted signal experiences increasing path loss at higher frequencies. As the received signal is transformed back to the time domain using inverse Fourier transform, the broadening effect appears clearly, in contrast to the originally transmitted delta function.

To quantitatively characterize the broadening effects in the THz Band, the auto-correlation of signals is needed. We define the *pulse duration*, t_d , as the time after which the auto-correlation stays below 0.1% of its maximum, which is equivalent to -30 dB interference to neighboring signals. This pulse

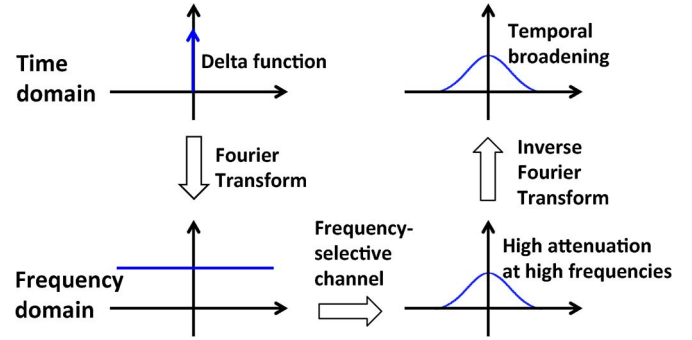


Fig. 6. An illustration for the temporal broadening effects.

duration suggests the minimum separation between consecutive pulses of transmission, to avoid ISI. Furthermore, we define the *broadening factor*, η , as the ratio between the pulse duration of the received pulse and that of the transmitted pulse. We analyze the broadening effects for both LoS and NLoS propagation, by transmitting raised-cosine pulses. This investigation is particularly useful when high-directivity antennas are being deployed and LoS path or directed NLoS is guaranteed. The broadening factor increases for higher center frequencies, wider pulse bandwidth and longer distances, due to the increases of the channel frequency-selectivity. The quantitative observations are discussed as follows.

- The broadening factor is closely related to the transmitted signal. In Fig. 7(a), the transmitted pulse occupies a bandwidth of 20 GHz and the pulse duration is $t_d = 120.4$ ps. The frequency-selective attenuation has broadening effects, and the broadening factor is smaller than 10. In Fig. 7(b), the 200-GHz-wide raised-cosine pulse with the duration $t_d = 10.6$ ps is transmitted. This wide pulse experiences a more severe frequency-selectivity and the resulting η exceeds 10 easily.
- The broadening factor depends on the center frequency. As the carrier frequencies increase from 0.3 THz to 0.7 THz, 1 THz and 2 THz, the broadening factors increase, because of more severe frequency-selectivity at higher frequencies in the THz Band. For example in Fig. 7(a), the average η is below 2 for $f_i = 0.3, 0.7$ and 1 THz. On the contrary, the average broadening factor is 3.75 when $f_i = 2$ THz. This suggests that to avoid ISI, a minimal 0.45 ns separation is required for the transmission of 20 GHz-wide pulses centered at 2 THz.
- As the communication distance increases, the frequency-selectivity in the THz Band becomes stronger and hence, more severe distortion arises on the received signals, as shown in Fig. 7(b). At $f_i = 0.3$ THz and 1 m, the broadening factor increases from 1.04 to 10.57, when the distance varies from 1 m to 10 m. Consequently, to avoid ISI, at least 0.11 ns spacing is needed between consecutive transmission, when the distance is 10 m, the center frequency is 0.3 THz and the transmitted raised-cosine pulse has a width of 200 GHz.
- The NLoS propagation affects the temporal broadening, as shown in Fig. 7(c). Without loss of generality, the reflected

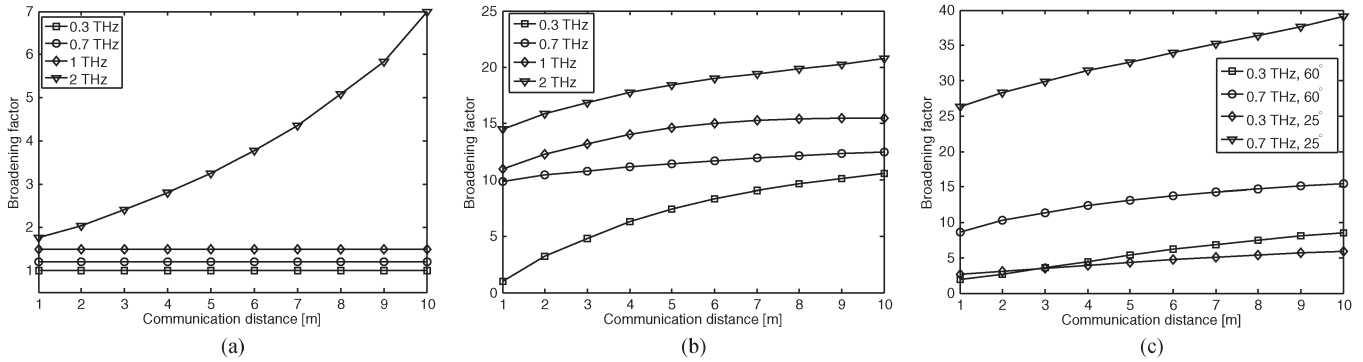


Fig. 7. Broadening factor analysis. (a) 20-GHz-wide pulse, LoS. (b) 200-GHz-wide pulse, LoS. (c) 200-GHz-wide pulse, reflected NLoS.

NLoS transmission is considered. For the same traveling distances and transmitted pulses, the reflection introduces additional loss as well as distortion on transmitted signals, particularly at higher frequencies. At 0.7 THz and $\theta_i = 25^\circ$, the reflection loss is -80 dB [see Fig. 2(b)] and the average broadening factor almost triples, increasing from 11.5 [see Fig. 7(b)] to 33.1.

E. Impact on Communication Techniques in the THz Band

These wideband channel characteristics coupled with the technology limitations, strongly affect the transmission techniques in the THz Band. The classical modulation schemes can be used for THz Band communication, but they will not be able to fully benefit the THz Band channel properties, such as the strong relationship between the distance and the bandwidth. In particular, three communication schemes are covered here, namely *impulse radio*, *distance-adaptive modulation*, and *multi-carrier transmission*.

First, the impulse radio techniques are developed for THz Band nano-networks [24], for its ultra-low complexity design. However, they are impractical for macro-scale applications, for the following reasons. By occupying the frequency spectrum up to several THz, this baseband scheme would interfere with the existing cellular networks operating in dedicated bands. Moreover, the occupation of the THz-wide bandwidth causes severe wideband broadening effects (as discussed in Section III-D), which strictly restrict the pulse rates. In particular, by occupying the entire THz Band, this impulse radio scheme experiences extreme frequency-selectivity. Although the pulse duration is 0.15 ps, the average broadening factor is 1319, which indicates a minimum separation of 0.19 ns between the neighboring pulses. This would result in the maximal pulse rate of 5.05×10^9 pulses-per-second to avoid ISI. Additionally, the synchronization for the extreme short pulses operating in the THz Band is extremely challenging, since it may require very high sampling rates (e.g., over multi-giga- or tera-samples per second).

Second, for distances longer than 1m, the molecular absorption defines multiple transmission windows, in which each window has a strongly distance-dependent bandwidth (as discussed in Section III-A). To utilize the advantages of the strong relationship between the bandwidth and the distance, a

new distance-aware adaptive modulation solution appears as an interesting path to explore. In this context, we developed a new modulation solution that allows the nodes to intelligently share the channel by adapting the modulation scheme dependent on the transmission distance [22]. In particular, a node can adaptively choose modulations based on the transmission distance to occupy either (i) the entire transmission bandwidth, (ii) the central part of the transmission window (this information reaches both close and far nodes), or (iii) the sides of the transmission window (the information only reaches nearby devices).

Third, the multi-carrier modulation permits adaptive transmissions of different symbols on non-overlapping sub-bands in parallel. As a result, each carrier occupies a smaller bandwidth (for example, 5 GHz as suggested in Section III-C) and supports lower data rates. This effectively relaxes the design requirements of individual carriers, and is helpful for THz Band communication to overcome ISI and can reach very high data rates. As compensation, many parallel modulators for different carriers and very fast signal generator to switch between carriers, are required to support multi-carrier modulation. Hence, the optimal sub-band width needs to be determined.

Consequently, based on the channel characteristics in the THz Band, distance-adaptive and multi-carrier transmissions are suggested to best benefit from the unique relationship between distance and bandwidth.

IV. CONCLUSION

In this paper, we have developed a unified multi-ray channel model in the THz Band by using ray tracing techniques. This multi-ray channel incorporates the propagation models for the LoS, reflected, scattered and diffracted paths, is validated by the experimental measurements (0.06–1 THz). Based on the developed propagation model, we presented a thorough analysis on the channel characteristics in the THz Band. Specifically, first, the spectral windows defined by the molecular absorption loss are distance-varying, and the width of these windows reduces as the distance increases. Second, the multipath wideband channel capacity can exceed 75 Gb/s with the use of 10 dBm transmit power and a water-filling power allocation strategy over 0.06–1 THz. This improvement of total path gain and capacity of the multipath propagation over LoS are at the cost

of the increased delay spread and consequently, the restricted coherence bandwidth to avoid ISI. Third, the rms delay spread is dependent on the distances and carrier frequencies. The resulting coherence bandwidth is below 5 GHz, which decreases for longer distances and lower carrier frequencies. Fourth, the temporal broadening effects limit the minimum spacing between consecutive transmission and hence the data rate. The defined broadening factor increases for higher center frequency, wider pulse bandwidth, longer distance, and is affected by the propagation path. Fifth, in terms of communication techniques, distance-adaptive and multi-carrier transmissions are suggested to best benefit from the unique relationship between distance and bandwidth. This work that addresses the unified multi-ray channel modeling and in-depth characteristic analysis lays out the foundation to design reliable and efficient communication systems in the THz Band.

REFERENCES

- [1] H. Song and T. Nagatsuma, "Present and future of Terahertz communications," *IEEE Trans. Terahertz Sci. Technol.*, vol. 1, no. 1, pp. 256–263, Sep. 2011.
- [2] R. Piesiewicz *et al.*, "Short-range ultra-broadband Terahertz communications: Concepts and perspectives," *IEEE Antennas Propag. Mag.*, vol. 49, no. 6, pp. 24–39, Dec. 2007.
- [3] I. F. Akyildiz, J. M. Jornet, and C. Han, "Terahertz band: Next frontier for wireless communications," *Physical Communication (Elsevier)*, vol. 12, pp. 16–32, Sep. 2014.
- [4] N. Moraitis and P. Constantinou, "Indoor channel measurements and characterization at 60 GHz for wireless local area network applications," *IEEE Trans. Antennas Propag.*, vol. 52, no. 12, pp. 3180–3189, Dec. 2004.
- [5] A. F. Molisch, "Ultrawideband propagation channels—Theory, measurement, modeling," *IEEE Trans. Veh. Technol.*, vol. 54, no. 5, pp. 1528–1545, Sep. 2005.
- [6] T. Kürner and S. Priebe, "Towards THz communications—status in research, standardization and regulation," *J. Infrared, Millimeter, Terahertz Waves*, vol. 35, no. 1, pp. 53–62, Jan. 2014.
- [7] S. Priebe, M. Kannicht, M. Jacob, and T. Kurner, "Ultra broadband indoor channel measurements and calibrated ray tracing propagation modeling at THz frequencies," *IEEE J. Commun. Netw.*, vol. 15, no. 6, pp. 547–558, Dec. 2013.
- [8] H. J. Song *et al.*, "Terahertz wireless communication link at 300 GHz," in *Proc. IEEE Top. MWP*, Oct. 2010, pp. 42–45.
- [9] K. Yasuko and S. Takamasa, "Terahertz-wave propagation model," *J. Nat. Inst. Inf. Commun. Technol.*, vol. 55, no. 1, pp. 73–77, 2008.
- [10] Y. Choi, J.-W. Choi, and J. M. Cioffi, "A geometric-statistic channel model for THz indoor communications," *J. Infrared, Millimeter, Terahertz Waves*, vol. 34, no. 7/8, pp. 456–467, Aug. 2013.
- [11] S. Priebe and T. Kurner, "Stochastic modeling of THz indoor radio channels," *IEEE Trans. Wireless Commun.*, vol. 12, no. 9, pp. 4445–4455, Sep. 2013.
- [12] J. Jornet and I. Akyildiz, "Channel modeling and capacity analysis for electromagnetic wireless nanonetworks in the Terahertz band," *IEEE Trans. Wireless Commun.*, vol. 10, no. 10, pp. 3211–3221, Oct. 2011.
- [13] R. Vaughan and J. B. Andersen, *Channels, Propagation and Antennas for Mobile Communications*. London, U.K.: IEE, 2003.
- [14] R. Piesiewicz *et al.*, "Terahertz characterisation of building materials," *IET Electron. Lett.*, vol. 41, no. 18, pp. 1002–1004, Sep. 2005.
- [15] R. Piesiewicz *et al.*, "Scattering analysis for the modeling of THz communication systems," *IEEE Trans. Antennas Propag.*, vol. 55, no. 11, pp. 3002–3009, Nov. 2007.
- [16] H. Ragheb and E. R. Hancock, "The modified Beckmann-Kirchhoff scattering theory for rough surface analysis," *Pattern Recognit.*, vol. 40, no. 7, pp. 2004–2020, 2007.
- [17] C. L. Vernold and J. E. Harvey, "Modified Beckmann-Kirchhoff Scattering Theory for Nonparaxial Angles," in *Proc. SPIE*, 1998, pp. 51–56.
- [18] R. G. Kouyoumjian and P. H. Pathak, "A uniform geometrical theory of diffraction for an edge in a perfectly conducting surface," *Proc. IEEE*, vol. 62, no. 11, pp. 1448–1461, Nov. 1974.
- [19] R. Luebbers, "Finite conductivity uniform GTD versus knife edge diffraction in prediction of propagation path loss," *IEEE Trans. Antennas Propag.*, vol. Ap-32, no. 1, pp. 70–76, Jan. 1984.
- [20] M. Jacob *et al.*, "Diffraction in mm and sub-mm wave indoor propagation channels," *IEEE Trans. Microw. Theory Techn.*, vol. 60, no. 3, pp. 833–844, Mar. 2012.
- [21] C. Jansen *et al.*, "Diffuse scattering from rough surfaces in THz communication channels," *IEEE Trans. Terahertz Sci. Technol.*, vol. 1, no. 2, pp. 462–472, Nov. 2011.
- [22] C. Han and I. F. Akyildiz, "Distance-aware multi-carrier (DAMC) modulation in Terahertz band communication," in *Proc. IEEE ICC*, 2014, pp. 5461–5467.
- [23] R. C. Qiu, C. Zhou, and Q. Liu, "Physics-based pulse distortion for ultra-wideband signals," *IEEE Trans. Veh. Technol.*, vol. 54, no. 5, pp. 1546–1555, Sep. 2005.
- [24] J. M. Jornet and I. F. Akyildiz, "Femtosecond-long pulse-based modulation for Terahertz band communication in nanonetworks," *IEEE Trans. Commun.*, vol. 62, no. 5, pp. 1742–1754, May 2014.



Chong Han (S'12) received the B.Eng. degree in electrical engineering and telecommunications from The University of New South Wales, Sydney, Australia, in 2011, and the master of science degree in electrical and computer engineering from Georgia Institute of Technology, Atlanta, GA, USA, in 2012. Currently, he is a Graduate Research Assistant in the Broadband Wireless Networking Laboratory (BWN Lab), School of Electrical and Computer Engineering, Georgia Institute of Technology. His current research interests include Terahertz band communication networks, Internet of Things, Internet of Nano-Things, Electromagnetic Nanonetworks, and Graphene-enabled Wireless Communication.



A. Ozan Bicen (S'08) received the B.Sc. and M.Sc. degrees in electrical and electronics engineering from Middle East Technical University, Ankara, Turkey, in 2010 and from Koc University, Istanbul, Turkey in 2012, respectively. He is currently a Graduate Research Assistant in the Broadband Wireless Networking Laboratory and pursuing the Ph.D. degree at the School of Electrical and Computer Engineering, Georgia Institute of Technology, Atlanta, GA, USA. His current research interests include wireless communication at the THz band, and molecular communication.



Ian F. Akyildiz (M'86–SM'89–F'96) received the B.S., M.S., and Ph.D. degrees in computer engineering from the University of Erlangen-Nurnberg, Germany, in 1978, 1981, and 1984, respectively. Currently, he is the Ken Byers Chair Professor in Telecommunications with the School of Electrical and Computer Engineering, Georgia Institute of Technology, Atlanta, GA, USA, the Director of the Broadband Wireless Networking Laboratory and Chair of the Telecommunication Group at Georgia Tech. He is an Honorary Professor with the School of Electrical Engineering, Universitat Politècnica de Catalunya (UPC), Barcelona, Catalunya, Spain and founded the N3Cat (NaNoNetworking Center) in Catalunya. Since September 2012, he is also a Finland Distinguished Professor Program (FiDiPro) Professor supported by the Academy of Finland at Tampere University of Technology, Department of Communications Engineering, Finland. He is the Editor-in-Chief of *Computer Networks Journal* (Elsevier), and the founding Editor-in-Chief of *Ad Hoc Networks Journal* (Elsevier), the *Physical Communication Journal* (Elsevier) and the *Nano Communication Networks Journal* (Elsevier). He is an IEEE Fellow (1996) and an ACM Fellow (1997). He received numerous awards from IEEE and ACM. His current research interests are in Terahertz band communication, nanonetworks, software defined networking, 5G cellular systems and wireless underground sensor networks.